2020

Domain Wall Conduction in Calcium-Modified Lead Titanate for Polarization Tunable Photovoltaic Devices

Chong-Xin Qian
Northwest University, Xi'an

Hong-Jian Hong-Jian
Northwest University, Xi'an, hjfeng@nwu.edu.cn

Qiang Zhang
Northwest University, Xi'an

Jiawei He
Northwest University, Xi'an

Zi-Xuan Chen
Northwest University, Xi'an

See next page for additional authors

Cell Reports
Physical Science

CellPress

Article

Domain Wall Conduction in Calcium-Modified Lead Titanate for Polarization Tunable Photovoltaic Devices

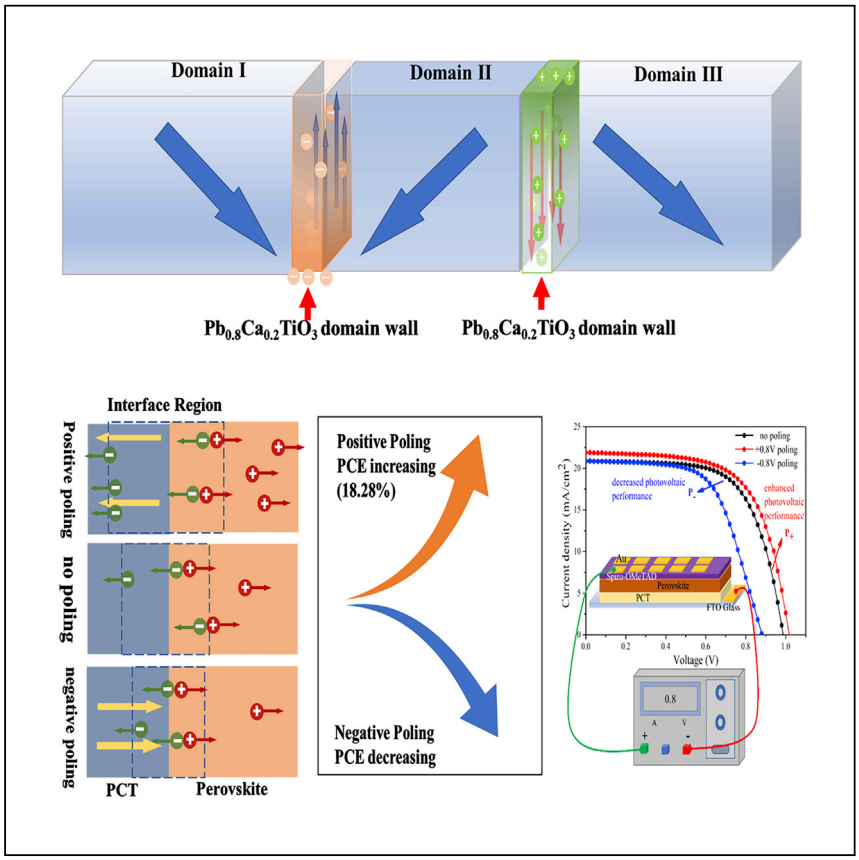

By virtue of the domain wall conduction and polarization tunable charge transport properties of ferroelectrics, Qian et al. theoretically demonstrate evidence of electric conduction in domain walls. They successfully fabricate $Pb_{0.8}Ca_{0.2}TiO_3$-based photovoltaic devices with tunable photovoltaic performance by external poling.

Chong-Xin Qian, Hong-Jian Feng, Qiang Zhang, Jiawei He, Zi-Xuan Chen, Ming-Zi Wang, Xiao Cheng Zeng

hjfeng@nwu.edu.cn,
fenghongjian@126.com (H.-J.F.)
xzeng1@unl.edu (X.C.Z.)

HIGHLIGHTS

Domain wall conduction in $Pb_{0.8}Ca_{0.2}TiO_3$ (PCT) is confirmed by DFT calculations

PCT-based devices with domain rearrangement tunable behavior are fabricated

Qian et al., Cell Reports Physical Science 1, 100043
April 22, 2020
https://doi.org/10.1016/j.xcrp.2020.100043

Cell Reports
Physical Science

CellPress

Article

Domain Wall Conduction in Calcium-Modified Lead Titanate for Polarization Tunable Photovoltaic Devices

Chong-Xin Qian,[1,3] Hong-Jian Feng,[1,3,4,*] Qiang Zhang,[1] Jiawei He,[1] Zi-Xuan Chen,[1] Ming-Zi Wang,[1] and Xiao Cheng Zeng[2,*]

SUMMARY

Ferroelectric domain wall (DW) conduction, confirmed in recent experiments, has attracted intense attention due to its promising applications in optoelectronic devices. Herein, we provide theoretical evidence of electric conduction in $Pb_{0.8}Ca_{0.2}TiO_3$ (PCT) DWs. The separation of charge accumulation in DWs, corresponding to the electronic conduction-band minimum (CBM) and valence-band maximum (VBM), weakens the tendency for the electron-hole recombination, thereby providing more efficient channels for charge transfer. We fabricate PCT-based functional photovoltaic devices with polarization tunable charge transfer to exploit the combined conduction and ferroelectric properties of the DW. The photovoltaic performance of the devices can be regulated by the alternation of ferroelectric domains in PCT, caused by variation of the external poling. Our work broadens the applicability of DW conduction and may inspire the future design of high-performance materials in photovoltaic devices.

INTRODUCTION

As a class of functional oxides, ferroelectric materials with spontaneous polarization and a series of excellent characteristics have been widely applied in ferroelectric field-effect transistors,[1] ferroelectric dynamic random-access memories, data storage, pressure sensing, and ultrasonic sensors.[2–6] Ferroelectric domain walls (DWs) are discontinuous regions of polarized charges between domains, which are often viewed as two-dimensional (2D) homointerfaces.[7,8] DWs can also be created, reshaped, and displaced by external electric fields,[9,10] a feature which is promising for future applications in electronic, spintronic, and optoelectronic devices. In particular, the discovery of enhanced conductivity of the localized metal-insulator transition,[11] the conductivity at phase boundaries[12] in complex oxides, the unexpected finding of the ferroelectric DW conductivity, and the enhancement of ferroelectric DW conductivity in wide bandgap semiconductors, including $BiFeO_3$,[13] $BaTiO_3$,[14] $LiNbO_3$,[15] and $PbZr_xTi_{1-x}O_3$,[16] have offered new avenues for developing DW-based nanoelectronics and drawn extensive research interest. The discovery of the enhanced electric conduction in DWs, especially in charged DWs,[17] calls for functional application of the conductive DWs. There are uncompensated positive or negative charges in the charged DWs, generating local electrostatic potential near the DWs. The latter potential is usually compensated for by the redistribution of free carriers, which further enhances the conductivity of the DWs.[18] In addition, large numbers of carriers tend to accumulate at the head-to-head charged DWs and form the depletion zone of donor ions, which results in the increase in conductivity at the DWs by several orders of magnitude.

[1]School of Physics, Northwest University, Xi'an 710069, China

[2]Department of Chemistry and Department of Mechanical and Materials Engineering, University of Nebraska-Lincoln, Lincoln, NE 68588, USA

[3]These authors contributed equally

[4]Lead Contact

*Correspondence: hjfeng@nwu.edu.cn, fenghongjian@126.com (H.-J.F.), xzeng1@unl.edu (X.C.Z.)

https://doi.org/10.1016/j.xcrp.2020.100043

Recently, ferroelectric materials have been studied as potential photovoltaic materials.[19–23] Ferroelectric polarization, induced by the broken space inversion symmetry of the ferroelectrics, can generate built-in fields, which can lead to band realignment across the ferroelectric-perovskite interface.[19] The direction of the charge transfer can be controlled by the poling direction of the ferroelectrics. Thus, ferroelectric materials can be introduced into perovskite solar cells (PSCs), serving dual roles of both ferroelectric tunable layer and electron transport layer to control the direction of carrier transportation. Ferroelectric polymers, such as poly(vinylidene fluoride) (PVDF), have been used as additives during the fabrication process to improve perovskite morphology and device performance.[20] Ferroelectrics-based PSCs exhibit ferroelectric tunable photovoltaic behavior associated with the rotation of the ferroelectric domains. Nevertheless, fewer studies have been reported for ferroelectric-based PSCs,[21] and also due to wide bandgap and insulator properties of ferroelectrics, their application as the electric transport layer (ETL) in PSCs is quite limited.[22] The electronic connectivity and charge transfer of the ETL can be improved to promote the transportation and extraction of charges to the electrode.[23] The incorporation of Ca into $PbTiO_3$ (PTO) leads to variation of geometric structure, and the enhancement of density of states of Ti 3d near the conduction-band minimum (CBM) gives rise to more channels for the charge transfer, while the large dispersion curvature near the CBM benefits the carrier migration. Therefore, the Ca-modified lead titanate solid solution, $Pb_{0.8}Ca_{0.2}TiO_3$ (PCT), becomes a promising candidate for combining the ETL and the ferroelectric tunable layer to further improve the photovoltaic performance of ferroelectric PSCs.

Today, the power conversion efficiency (PCE) of organic metal halide PSCs has reached 25.2%.[24] Planar heterojunction PSCs commonly use low-temperature prepared TiO_2 as the ETL with desirable device performance, owing to the suitable energy levels, non-toxicity, and low-cost preparation method of TiO_2.[25–31] However, TiO_2 thin film prepared at low temperature possesses low-electron mobility and numerous surface defects, often leading to charge accumulation at the perovskite-TiO_2 interface.[32,33] In photovoltaic device, in general, the built-in field is the main force to drive the carriers drifting toward corresponding electrodes and to avoid carrier recombination.[34] To enhance the built-in field and suppress the carrier recombination in the trap states, a sensible approach reported recently is to apply an external electric field to the photoactive layer, resulting in a strong and stable polarization.

Here, we apply theory to study the conduction behavior in 90° PCT DWs. The separation and accumulation of charges near the DWs demonstrate the enhancement of DW conductivity, suggesting DWs as efficient charge transfer channels. The measured DW conductivity reaches $\sim 2.8 \times 10^{-3}$ S/cm, which is higher than the conductivity of TiO_2 (8.32×10^{-4} S/cm), further confirming good DW conduction. Moreover, the photovoltaic performance can be regulated by external poling, demonstrating the polarization tunable charge transfer property of PCT-based devices. To achieve enhanced photovoltaic properties of the PCT-based device, we incorporate a modified layer into the PCT-based device.

RESULTS

Understanding and Confirming the Ferroelectric DW Conduction

Considering that the ferroelectricity of PCT resulted from the off-centering displacement of Ti with respect to the center-symmetric structure, we theoretically build 90° DW models with different atomic layers to simulate the experimentally

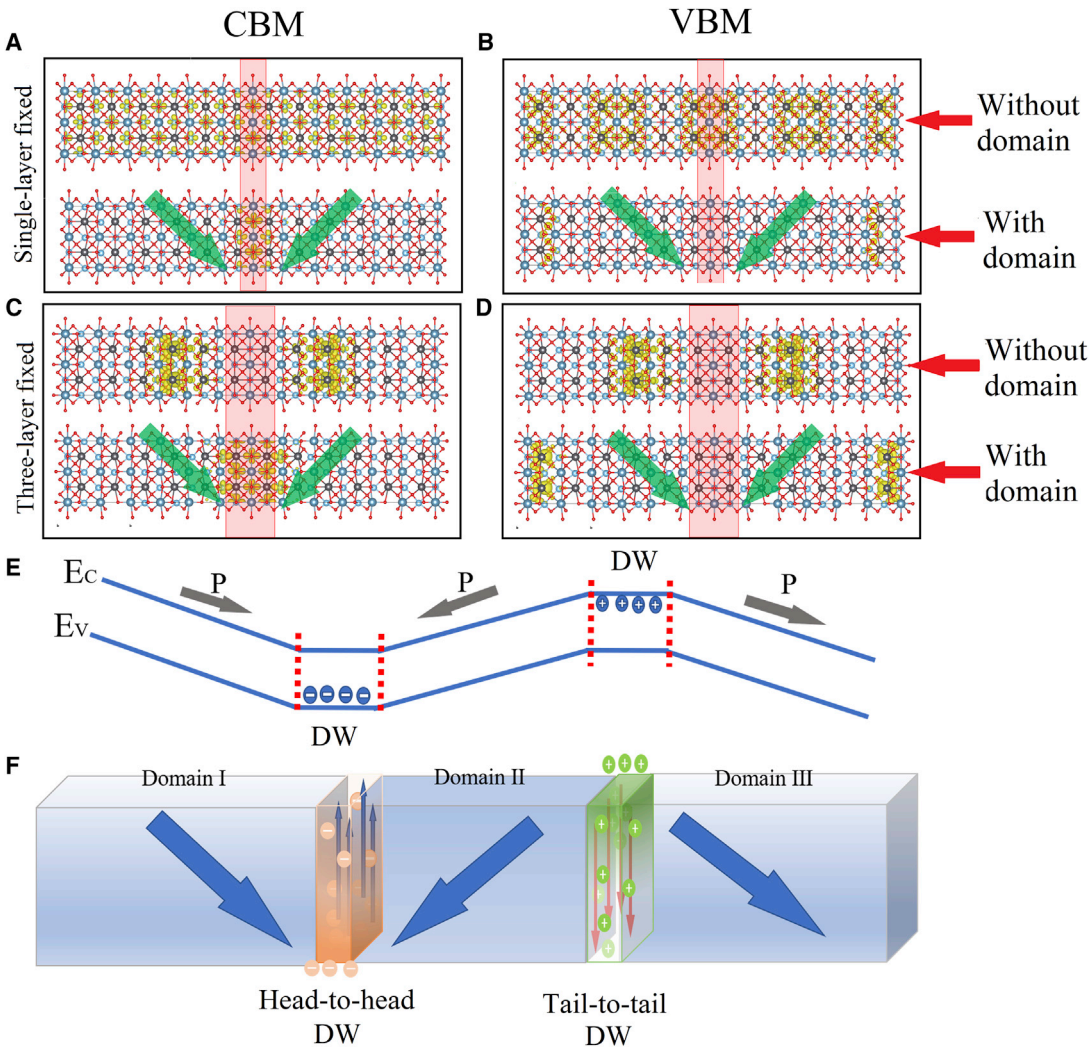

Figure 1. Calculation of the Ferroelectric Domain Wall (DW) Conduction

(A–D) The charge density corresponding to CBM for (A) single-layer and (C) three-layer without domain and 90° DW structures (highlighted in red strip). The charge density corresponding to VBM for (B) the single-layer and (D) the three-layer without domain and 90° DW structures. The yellow iso-surface represents a charge density of 0.001 e/Å^3, and the arrow denotes the polarization direction of each domain.

(E) The energy band diagram of 90° DWs associated with different charge accumulation.

(F) A schematic of charge accumulation at different DWs.

verified behavior of the DW conduction (see below; the measured conductivity amounts to ~2.8 × 10^{-3} S/cm). Here, the Ti atoms are artificially shifted by 0.2 Å along the polarization axis, resulting in the head-to-head DWs. For the structures without the domains (see Figure 1), the computed charge densities corresponding to the CBM and valence-band maximum (VBM) are evenly distributed over the entire supercell. To study the DW conduction and charge transfer, single-layer and three-layer 90° DW models are used. As shown in Figures 1A and 1C, the localized charge density corresponding to the CBM is around the head-to-head DW region, indicating electron accumulation at the head-to-head DW. Figures 1B and 1D display the computed charge density corresponding to the VBM for the single-layer and the three-layer 90° DW models, respectively. With the increase in the DW thickness, a more localized charge density distribution corresponding to the CBM is seen in the head-to-head DW region. It is worth noting

that the charge density distribution corresponding to the VBM is constrained near the tail-to-tail DW, suggesting the hole accumulation at the tail-to-tail DW.

Figure 1E shows the polarization of ferroelectric domains results in clear band bending and band alignment at head-to-head DWs, while the tail-to-tail DWs result in the reversal of band alignment, leading to the electron and hole carrier separation and accumulation in the corresponding DW regions. Figure 1F describes the mechanism of charge transfer at 90° DWs. The head-to-head DWs provide efficient electron transfer channels, while the tail-to-tail DWs tend to enhance the hole transfer. The separation of the positive and negative charge carriers in DWs hinders the electron-hole recombination and provides efficient channels for charge transfer to further improve the DW conduction. The higher carrier mobility of electrons leads to higher electric conductivity of the head-to-head DWs than the tail-to-tail DWs, consistent with the experimentally measured results.[14]

To further verify the DW conduction by experiments, we fabricated a PCT thin film and measured the conductivity using a four-probe conductivity meter. The measured conductivity of PCT thin film amounts to $\sim 2.8 \times 10^{-3}$ S/cm, much higher than the conductivity of TiO_2 (8.32×10^{-4} S/cm),[35] confirming the high electric conduction across the DWs. The experimentally confirmed high conductivity of PCT thin film and the theoretical evidence of DW conduction above suggest the likelihood of achieving local conductivity in ferroelectrics and of making devices based on DWs.

Experimental Characterization of Microstructure and Ferroelectric DWs of PCT Films

To examine the ferroelectricity change in PCT thin film, we studied the spontaneous polarization of the PCT. Transmission electron microscopy (TEM) images of ferroelectric PCT grains with domain structures are shown in Figures 2A–2D, where the red arrows denote the DWs. Figure 2D displays the high-resolution TEM (HRTEM) image near the yellow dashed line regions shown in Figure 2C. The location of the DWs can be determined from the fast Fourier transforms (FFTs) of the both sides of the DWs, as shown in Figures 2E–2G. The DW is along the [101] plane, and the rotation between two domains is reflected in the splitting of the diffraction peaks.[36–39]

The measured polarization versus voltage hysteresis loop for the PCT film is shown in Figure 3A, giving a strong evidence of the existence of the ferroelectric polarization of the PCT film upon external poling. To investigate the ferroelectric domain distribution under alternating tip biases in the different regions, we scanned the vertical piezo-response force microscopy (PFM) signals of the PCT film over an area of $2 \times 2\ \mu m^2$, and the schematic diagram of the PFM is shown in Figure 3B. To complete a piezoelectric image, the topography, the amplitude, and the phase parameters must be carefully monitored, as shown in Figure 3C. The topographic image of the PCT film does not show any surface deformation after these procedures. The amplitude image reveals the relative strength of the piezoelectric coefficient, and the phase image represents the direction of the polarization.

With the tip biases changing from 0 to ± 12 V, the grain polarizations tend to orient consistently, which presents as a typical grain-like domain structure (see Figure S1). Therefore, the results present a strong evidence for the switchable and stable polarization in the PCT thin film. The PFM phase image indicates that a positive driving voltage (up to 12 V) causes significant phase changes (i.e., creating more out of-phase domains), more than applying a negative driving voltage. It means

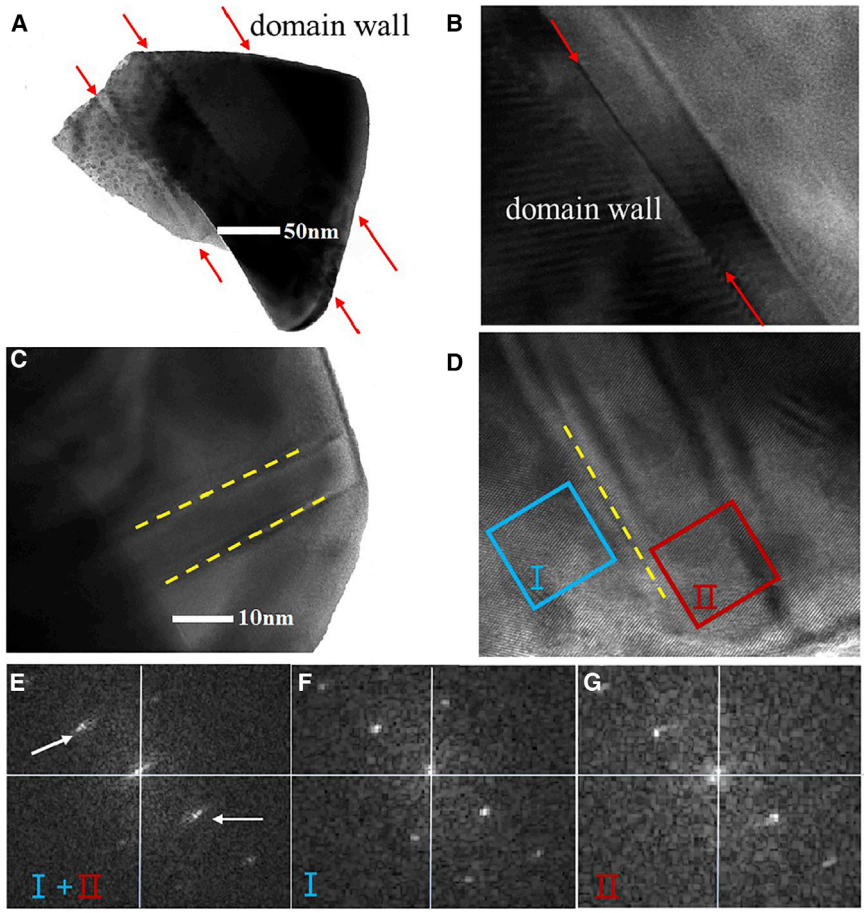

Figure 2. Ferroelectric DWs' Characterization of PCT Films with TEM

(A and B) Representative bright-field TEM images (A) a large crystalline grain and (B) local amplification of grains of the PCT with domain structures, where the domain walls are indicated by red arrows. Scale bar, 50 nm.

(C) HRTEM images with two domain regions marked by yellow dashed lines. Scale bar, 10 nm.

(D) Enlarged HRTEM image of the yellow DW area in (C).

(E–G) FFTs of (F) blue and (G) red squares in (D) and (E) their summed images. The white arrows in (E) mark a characteristic peak splitting due to the formation of domains.

that before applying the voltage, most of the domains point upward to the scanned surfaces. In addition, when the positive driving voltage is applied to the PCT samples, the obvious ferroelectric domain inversion can be seen from the phase diagrams, indicating that the ferroelectric domains can be rearranged with the variation of external bias. The redistribution of local ferroelectric domains induced by the alternative external bias in PCT thin films shows that the ferroelectric polarization can actuate the interaction between ferroelectric domains and photogenerated carriers, which inhibits or promotes the charge transfer across the PCT-perovskite interface. Therefore, PCT, as a functional layer, can control the direction of charge transfer to improve the performance of PSCs.

Electronic and Structural Connectivity of PCT

To confirm that PCT can improve the performance of ferroelectrics-based photovoltaic devices, we computed the electronic and structural properties of PCT using density functional theory (DFT) methods. The electronic band structure of PCT calculated based on the Perdew-Burke-Ernzerhof (PBE) functional is shown in Figure S2.

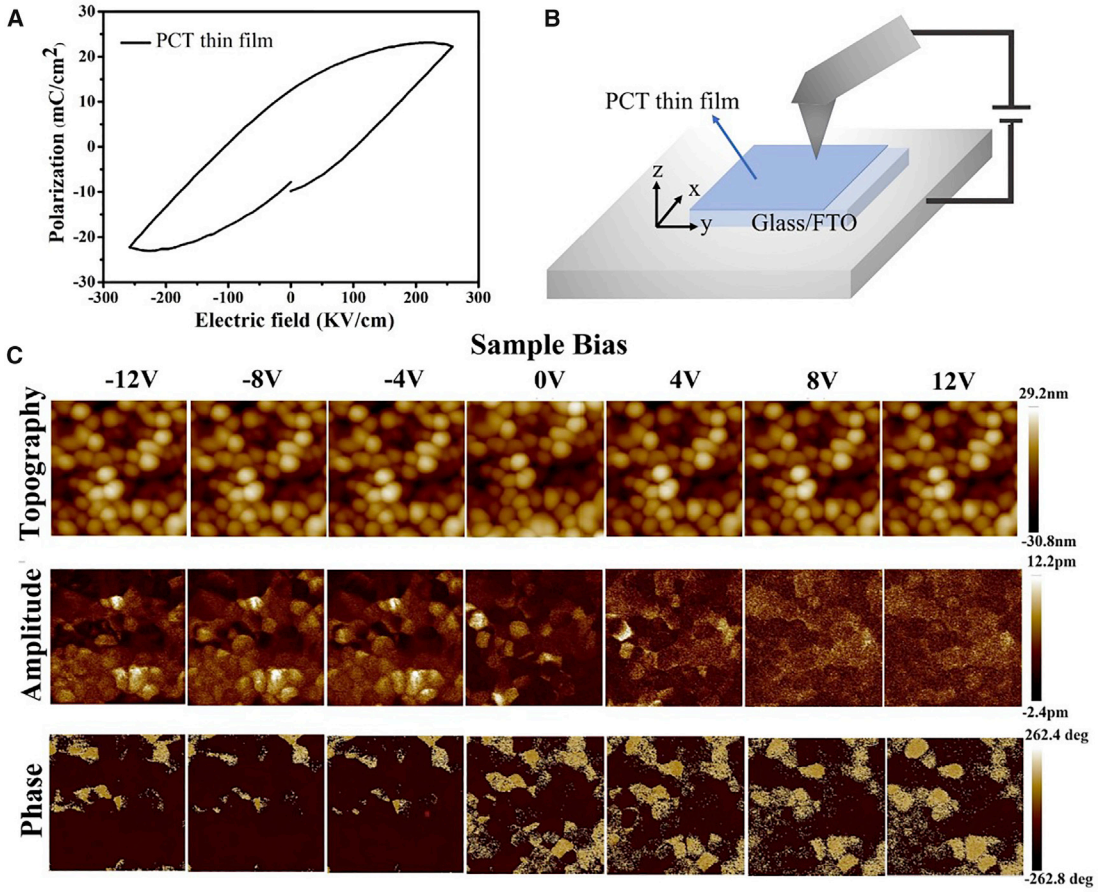

Figure 3. Ferroelectric DWs' Characterization of PCT Films with PFM

(A) The polarization versus voltage hysteresis loop for the PCT thin films.

(B) The schematic diagram of PFM scanning on PCT film, with the different current directions at the top contact area.

(C) The PCT film surface topography, amplitude, and the phase images under the bias voltage arrange from 0 to ±12 V, respectively.

The Heyd-Scuseria-Ernzerhof (HSE06) functional is also used to provide a more accurate band gap, as the PBE functional tends to underestimate the band gap of semiconductors (Figure 4A). Compared to the PTO, which has an indirect band gap of 3.23 eV, PCT possesses a slightly narrow indirect band gap of 3.12 eV. The relatively large dispersion curvature near the CBM suggests a small, effective mass of electrons, which benefits the carrier migration due to low energy loss, while hindering nonradiative recombination.

The charge density corresponding to CBM and VBM is presented in Figures 4B and 4D. The CBM is mainly contributed by the Ti 3d orbital, while the O 2p orbital mainly contributes to the VBM. A 2D sectional image of the charge density corresponding to CBM, projected onto the (010) plane, and that to VBM, projected onto the (001) plane (Figures 4C and 4E), also clearly show the contribution to CBM by the Ti 3d orbital and to VBM by the O 2p orbital, as well as the electronic and structural connectivity between the Ti-O cage of PCT and the Pb-I cage in the halide perovskite (Figure 4F). The similar structure between PCT and halide perovskite, and thus the desirable electronic and structural connectivity, tends to enhance the photovoltaic performance of PCT-based PSCs, resulting in improved charge transport (Figure 4F). The incorporation of Ca in PCT leads to a variation in geometric structure, the

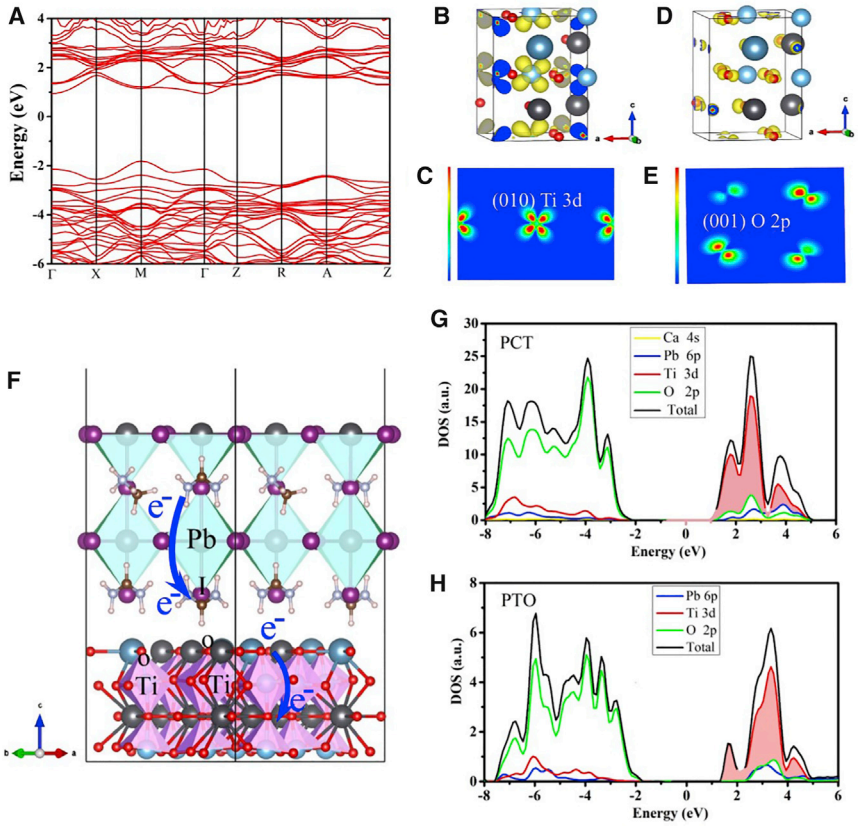

Figure 4. Electronic and Structural Connectivity of PCT

(A) Electronic band structure of PCT, calculated based on the HSE06 functional.

(B–E) Charge density corresponding to (B) CBM and (D) VBM of PCT. 2D sectional images of (C) the (010) plane for charge density corresponding to CBM and (E) the (001) plane for charge density corresponding to VBM of PCT.

(F) A schematic diagram of electronic and structural connectivity across the PCT-perovskite interface.

(G and H) The total and partial density of states projected onto the individual atoms of (G) PCT and (H) PTO, calculated based on the HSE06 functional.

electronic structure for TiO_6 octahedron, and the bonding feature between Ti and O atoms. The total and partial density of states (DOS) of PCT and PTO, calculated based on the HSE06 functional, are shown in Figures 4G and 4H, respectively. Compared with the PTO, the DOS of the Ti 3d orbital of PCT near the CBM increases significantly, implying an enhanced charge transfer channel and the capability of PCT for charge extraction as a good ferroelectric tunable layer and electron transport layer. Furthermore, the projected DOS peak of Ti 3d near the CBM exhibits enhanced intensity with respect to the second DOS peak of Ti 3d in the conduction band of PCT, compared to that of PTO. The Ca doping in PTO also increases the broadening of the DOS peak of Ti 3d near the conduction band edge, resulting in higher DOS around the CBM. The enhancement of the DOS of Ti 3d near the CBM gives rise to more channels for the charge transfer, leading to a faster charge-transfer rate in PCT-based devices.

Experimental Testing of Photovoltaic Performance of the PCT-Based PSCs upon Poling

The off-center displacement of the Ti atom in PCT is responsible for the spontaneous polarization of ferroelectric domains upon external electric fields (see

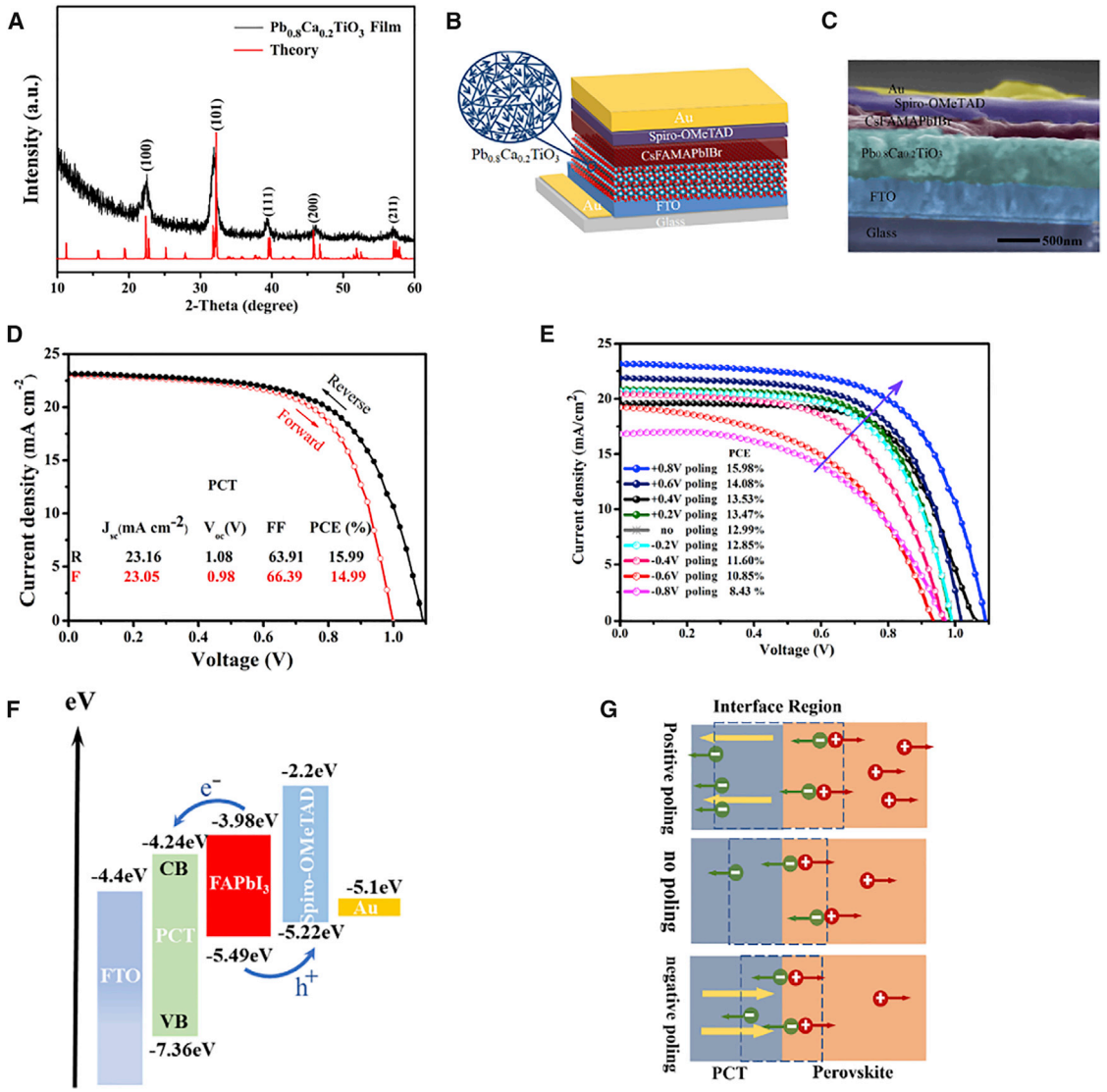

Figure 5. Device Structure and Photovoltaic Performance

(A) XRD pattern for the PCT film.

(B) Structure schematics of the ferroelectric-based perovskite solar cell (PSC) devices. The amplified diagram shows the spontaneous polarization of PCT ferroelectrics.

(C) A cross-sectional SEM image of a complete device based on bare PCT ETLs.

(D) The J-V curves of the device with PCT, measured under both reverse and forward scan directions.

(E) J-V curves of the devices based on PCT ETLs without poling and with different poling, respectively. The direction of the arrow indicates an increase in PCE.

(F) Energy-level diagram of the PCT devices, exhibiting the collecting process of photogenerated charge carriers.

(G) Schematic diagram of the carrier transport mechanism across the interface between PCT and perovskite, upon positive and negative poling. The yellow arrow indicates the direction of ferroelectric polarization.

Figure S3). X-ray diffraction pattern (XRD) measurement confirms the formation of the perovskite phase of PCT. The uniform and pure phase PCT film was obtained (Figure 5A). Figure S4 shows the optical spectra of PCT coated on fluorine-doped tin oxide (FTO), a sample displaying high transmittance in the visible light region to facilitate the light absorption of the devices. We introduced the PCT as the ferroelectric tunable layer and electron transport layer into our PSCs with the architecture FTO/PCT/$Cs_{0.05}FA_{0.8}MA_{0.15}Pb(I_{0.85}Br_{0.15})_3$/Spiro-OMeTAD/Au, as is shown in Figure 5B.

To gain a deeper understanding of the ferroelectric domain behavior upon poling, we further investigated the ferroelectric characteristics and optical properties of PCT films. The cross-sectional scanning electronic microscopy (SEM) images illustrated in Figure 5C show the morphology of the complete devices. The thicknesses of the perovskite layer and the Spiro-OMeTAD layer are 300 and 150 nm, respectively. The PCT film was introduced as the ETL, while the $Cs_{0.05}FA_{0.8}MA_{0.15}Pb(I_{0.85}Br_{0.15})_3$ halide perovskite film was the light absorber. We measured the device performance of PCT-based PSCs under reverse and forward scan. The J-V curves show no appreciable hysteresis under two different scan directions (Figure 5D). Reverse and forward scans show the PCE of 15.99% and 14.99%, respectively, and the average efficiency is ~15.49%. To study the influence of ferroelectric polarization on the device performance, we applied a series of appropriate bias, ranging from −0.8 to +0.8 V, on the devices. Figures 5E and S5 display J-V curves of PCT-based PSCs with the key parameters, including short-circuit current density (J_{sc}), open circuit voltage (V_{oc}), fill factor (FF), and PCE. The PCE increased significantly from 12.99% to 15.98% with the +0.8 V positive poling. These parameters are notably increased with the increase in the positive poling voltage, indicating that the PCT can improve the separation and extraction of photogenerated carriers under positive polarization states (see Table S1). The energy-level alignment (Figure 5F) indicates that the lower work function of the PCT inserted between the FTO and the perovskite absorber effectively decreases the interface barrier, facilitating the electron collection. The conduction band offset of the perovskite/PCT heterostructure is determined to be ~0.26 eV, which was calculated based on the HSE06 functional with respect to the vacuum level (see Figure S6). Electrons in the valence band are excited into the conduction band to form photoinduced carriers, which are further separated and extracted by ETL under illumination. After positive poling, ferroelectric polarization formed in the PCT film strengthens the built-in field of PSCs to improve the separation and extraction of carriers at the interface of the PCT-perovskite heterostructure. Conversely, the opposite ferroelectric polarization is responsible for the reduction in charge extraction, while the polarization weakens the built-in field of PSCs in this case (Figure 5G). In addition, the interface states lead to interfacial carrier tunneling, which further promotes charge extraction and photovoltaic performance, as discussed in detail in our previous work.[21]

Mechanism of Ferroelectric Tunable Charge Transfer and Photovoltaic Performance of PCT-Based PSCs

The interfacial charge transfer between the PCT and halide perovskite layers was investigated to gain deeper insight into the ferroelectric tunable behavior and the improvement of PSCs due to the electronic behavior associated with the ferroelectric polarization of PCT upon external poling. PCT and halide perovskite exhibit nearly the same perovskite structure, with relatively small lattice mismatch (~2.5%) and weak distortion within the interface of the heterostructures. We built six different interfaces to optimize. We chose the TiO-FAI heterostructure since it has the lowest interfacial formation energy (see Figure S7). The charge density (corresponding to VBM and CBM) of this heterostructure under different polarization is shown in Figures 6A and 6B, respectively. Under the positive poling, the charge density corresponding to the CBM is pushed away from the interfacial region, leading to decreased overlap between the CBM and the VBM, which lowers the rate of carrier recombination and the nonradiative recombination. A large portion of charge density corresponding to the CBM moves deeply to the PCT ETL, confirming the tunable and enhanced photovoltaic performance of PCT-based PSCs in our experiment. Under the negative poling, in contrast, the charge density corresponding to

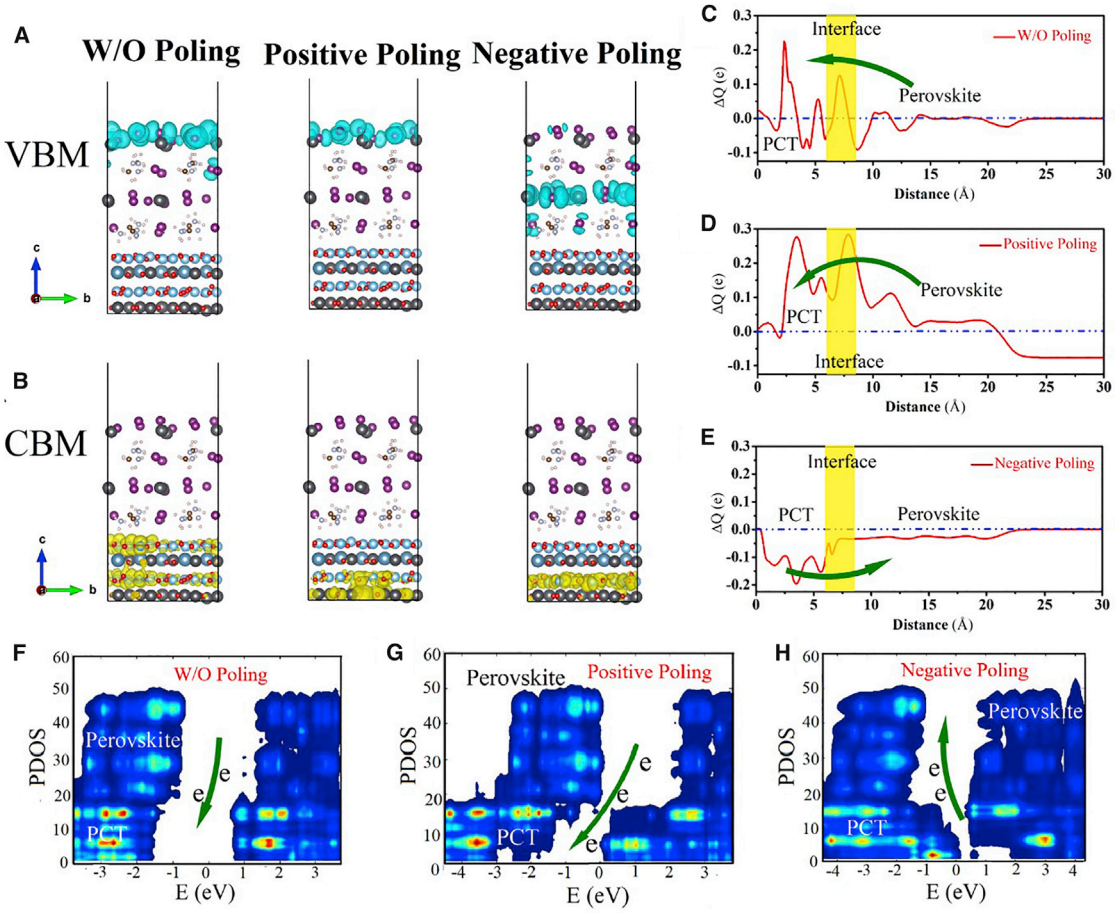

Figure 6. Ferroelectric Tunable Charge Transfer and Photovoltaic Performance

(A and B) Charge density corresponding to (A) VBM and (B) CBM of the PCT-perovskite heterostructure without poling, or under positive poling or negative poling. The yellow or blue iso-surfaces represent the charge density of 0.0004 e/Å^3.

(C–E) The charge displacement curves of PCT-perovskite heterostructure with (C) without (D) positive (E) negative poling conditions. The yellow area is the interface region between PCT and perovskite.

(F–H) The integrated local density of states projected along the < 001 > direction for PCT-perovskite interface upon (F) without (G) positive (H) negative poling conditions.

the VBM moves to the interfacial region, which lowers the photoinduced carrier lifetime and leads to the notorious nonradiative recombination, thus hindering the efficient charge transfer and decreasing the photovoltaic performance of the PSCs. The variation of charge distribution upon different poling conditions reflects the underlying mechanism of the ferroelectric tunable photovoltaic performance of PCT-based PSCs, which is consistent with the experimental results.

The charge displacement curve (CDC) ΔQ between the lowest triplet states and ground states can be used to further examine the mechanism of interfacial charge transfer at a one-electron excited state upon different poling conditions (Figures 6C–6E).[40] To this end, we set up different direction polarization by moving Ti^{4+} cations with the same displacement, along the direction that is perpendicular to the interface of the heterostructure to simulate the negative and positive poling in our DFT calculations. The ΔQ was calculated by integrating the average charge difference along the direction perpendicular to the interface, in which positive value represents the charge being transferred from right to left at the point of the CDC,

while the negative value indicates the opposite charge transfer behavior. The positive gradient implies that the charge is accumulating in that region, while the negative gradient indicates the depletion of the charges in that region. Without the poling, the ΔQ in the interface region is positive, indicating the charge transport from perovskite to PCT. Unfortunately, the value is negative near the interface of the PCT, and this causes an accumulation of photoinduced electrons in the interface region, which affects the charge transfer. Under positive poling, the CDC values across the whole heterostructure are positive, reflecting high charge transfer from halide perovskite to the PCT side and enhancement of the photovoltaic performance. Under negative poling, the value of CDC is reversed compared with positive poling, and the values in the entire region are negative, indicating the undesired charge transfer from the PCT side to halide perovskite, which results in poor charge transfer and photovoltaic behavior in the devices. All of the CDC analyses agree well with our PSC performance upon alternating external poling voltage.

To further confirm the tunable charge flow pathway and charge transfer, the integrated local DOS (LDOS) projected along the < 001 > direction perpendicular to the interface upon different poling conditions is illustrated in Figures 6F–6H. The reversal of type II band alignment for the PCT-perovskite heterostructure before and after exerting poling can be observed clearly. Without the exerting external bias, the type II band alignment favors charge transfer from the perovskite side to the PCT layer. Under positive poling conditions, the larger gradient distribution states of the conduction band alignment across the interface tend to promote the electron flow from the perovskite to the PCT layer, which is reasonable for the effective charge extraction and enhanced photovoltaic performance. The negative poling causes the reversed gradient distribution states of valence band and conduction band across the interface, thus hindering charge extraction and transportation. We therefore conclude that the rearrangement and reversal of band alignment across the PCT-halide perovskite interface upon alternating poling are the driving forces and can be attributed as the mechanism for the PCT-based PSCs. From the discussion above, the charge transfer, charge density distribution, and type II band alignment are consistent with the conclusion that the ferroelectric PCT can regulate the charge extraction and separation at the interface, leading to polarization tunable device performance.

Experimental Testing of Photovoltaic Performance and Stability of PSCs Based on Different ETLs

With the superior optoelectronic properties and the ferroelectric polarization behavior discussed above, it is expected that the PCT modified by TiO_2 would make an even better ETL in the PSCs than pure PCT. To confirm this, mesoscopic-type PSCs are designed and fabricated based on PCT and TiO_2-PCT ETLs with the aforementioned structure. The control sample based on TiO_2 was also prepared. Figure S8 presents the optical transmission spectra of these different ETLs deposited on the glass-FTO substrate. Due to the low reflection, PCT and TiO_2-PCT display higher transmittances in the wavelength range of 300–800 nm than the commonly used TiO_2 film, promoting the incident light absorption for high-efficiency solar cells. To further demonstrate the device characteristics, the photocurrent density of the champion devices based on PCT, TiO_2, and TiO_2-PCT was measured.

Figure 7A presents the measured J-V curves of mesoscopic-type PSCs, and the relevant parameters are listed in Table S2. The measured PCEs of the champion devices based on PCT, TiO_2, and TiO_2-PCT stabilize at 15.99%, 17.51%, and 18.28%, with the photocurrent densities of 23.16, 20.74, and 23.11 mA/cm^2, respectively. In

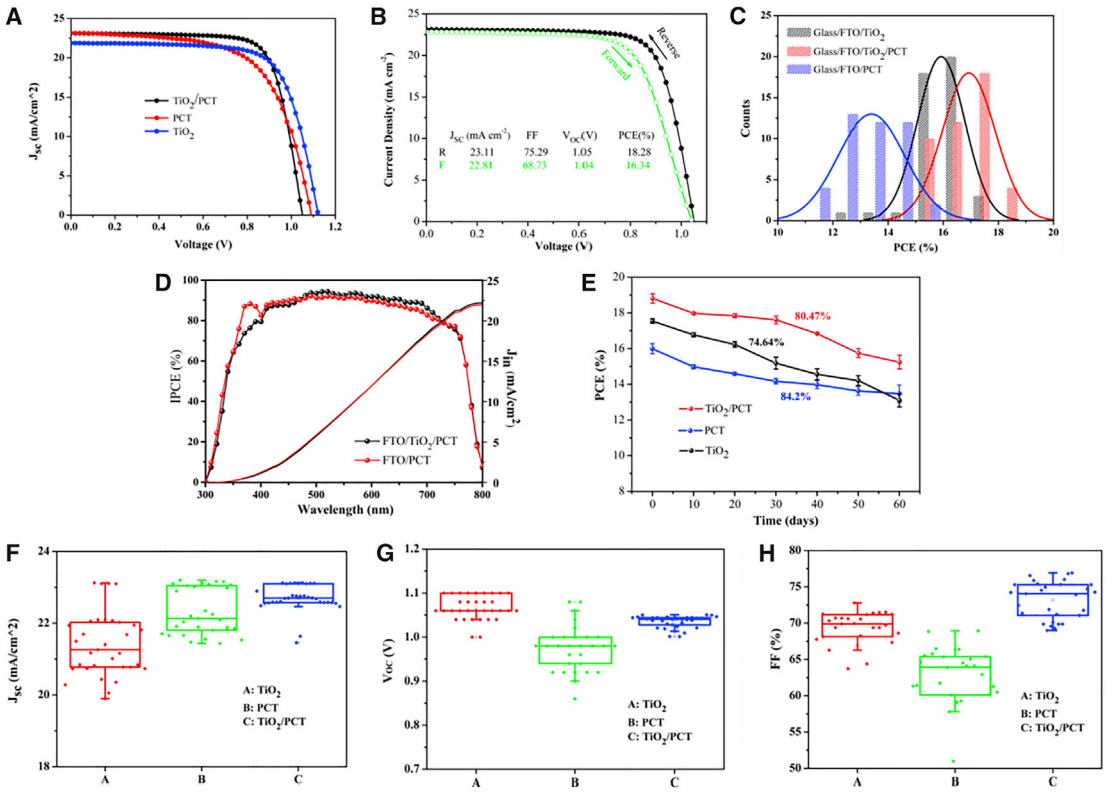

Figure 7. Photovoltaic Performance of Devices

(A) J-V characteristics of the solar cells based on PCT, TiO_2-PCT, and TiO_2.

(B) J-V curves of the champion devices based on TiO_2-PCT measured under both reverse and forward scan directions.

(C) PCE distribution histogram of the mesoscopic-type PSCs based on different ETLs.

(D) The corresponding EQE of the mesoscopic-type PSCs with various ETLs. The integrated current density from the EQE curves with the AM1.5G photon flux spectrum.

(E) Long-term stability measurements of devices without any encapsulation under ambient conditions at room temperature. The error bars are defined as the standard deviation for six devices.

(F–H) Statistics of device performance J_{sc} (F), V_{oc} (G), and FF (H), and of PSCs with TiO_2, TiO_2-PCT and PCT as ETLs, respectively. The median and mean are represented by the line dividing the boxes and the open square symbols, respectively. The cross symbols represent the maximum and minimum values.

all cases, the modified devices notably outperform the control device. The J-V curves of the champion devices based on TiO_2-PCT measured under both reverse and forward scan directions are shown in Figure 7B. The hysteresis is ascribed to the interfacial capacitance formed by charge accumulation at the interface, which is originally caused by ion migration, high interfacial trap density, and charge imbalance in the perovskite heterostructure.[41,42] Compared to the pure PCT devices, the device hysteresis of TiO_2-PCT was smaller, suggesting that the TiO_2 modification can reduce the trap density at the interface. Figure 7C shows the PCE value (reverse scan direction) statistical distribution histogram for 60 devices of all 3 ETLs. The DWs of the PCT layer can be viewed as the grain boundary with high chemical activity and may cause the decomposition of the perovskite layers to lead to the instability of the devices. We measured the lifetime and the PCE of the passivated PCT-based devices with interface engineering. To suppress the side effect caused by the DWs of the PCT layer, the contact of the PCT layer with the perovskite layer is prohibited by the interface engineering approach. For the surface passivation of PCT film, the [BMIM]BF4-IL dissolved in anhydrous ethanol (3 mg/mL) was spin coated on the PCT layer of the devices. The passivated devices were stored in dry containers under

45% relative humidity at room temperature for >6 months. It is worth noting that the passivated PCT-based devices exhibit high stabilities in the environment, and the highest PCE can still reach 15.77%, which is enough to prove the acceptable lifetime and durability of the passivated PCT-based devices (see Figure S9). The devices based on TiO_2-PCT also exhibit excellent reproducibility and high efficiency, with a very low standard deviation compared with the devices based on PCT and TiO_2, indicating that the TiO_2-modified PCT is an excellent ETL for the mesoscopic-type PSCs. In general, the minimum series resistance (R_s) and maximum shunt resistance (R_{sh}) values of the two devices with different ETLs are statistically analyzed to further investigate interfacial carrier recombination. Compared with the TiO_2-based device, the PCT-based device possesses smaller R_s and higher R_{sh}, indicating the inhibited carrier recombination across the interface (see Figure S10).

Furthermore, typical external quantum efficiency (EQE) and the integrated current density of PCT and TiO_2-PCT-based solar cells are shown in Figure 7D. In the visible light region, the EQE can reach up to 93% and 91%, and the integrated short circuit current is 22.27% and 22.05% mA/cm^2 for the respective devices, which are very close to the J-V results. It is apparent that the device based on TiO_2-PCT shows significantly higher EQE due to less optical loss when perovskite is deposited on TiO_2-PCT ETLs. The environmental stability of the corresponding solar cells was further evaluated, and the bare devices were exposed under 45% relative humidity at room temperature for 1,440 h (Figure 7E). It is worth noting that the TiO_2-modified PCT and the PCT-based devices exhibit higher stabilities in the environment, and the PCE of the PCT-based device remains at 84.2% of the initial value, while that of the TiO_2-based device degrades notably under the same environmental conditions. This may be attributed to the same perovskite structure between PCT and the halide perovskite, thus less trap density in the ferroelectric PCT layer, and to the electronic channel formed by interfacial ionic interaction between PCT and halide perovskite, which provides strong resistance to degradation during long-term use. To systematically study the performance of different ETL-based devices, 34 datasets of J_{sc}, V_{oc}, and FF from these devices were collected and are presented in Figures 7F–7H. The results confirm that the ferroelectric PCT layer has a favorable structural and electronic connectivity with the halide perovskite light-absorbing layer for the electron extraction. Thus, application of the ferroelectric tunable ETL in the ferroelectrics-based photovoltaic devices appears to be an effective material design strategy.

DISCUSSION

In conclusion, we provide theoretical evidence for DW conduction in 90° PCT DWs. By means of the TEM and PFM measurements, we identify a large ferroelectric domain on the PCT crystal grain and the ferroelectric domain reversal under the external electric field, demonstrating the existence of DWs. More importantly, the desirable electric conductivity of PCT thin film indicates the DW conduction. With the combination of DW conduction and ferroelectricity, we design a new PCT-based photovoltaic device with polarization tunable charge transfer. DFT computation was also used to obtain the CDC of the simulated excited states and the charge distribution corresponding to CBM and VBM across the PCT-perovskite heterojunction upon different poling conditions. The calculation results of the CDC in the triplet state and the charge distribution indicate that the excellent electronic and structural connectivity between PCT and perovskite favors the charge transfer and extraction and can decrease the nonradiative recombination center. Lastly, we successfully fabricate the PCT-based functional photovoltaic devices with polarization tunable

charge transfer and further incorporate a modified layer into PCT-based devices to achieve enhanced photovoltaic properties. The marked enhancement not only broadens the applicability of the DW conduction in photovoltaic devices but also assists in the future design of high-performance photovoltaic materials.

EXPERIMENTAL PROCEDURES

Fabrication of the PCT Film

To prepare the stable yellow-colored PCT sol-gel precursor solution, 0.35 g calcium acetate and 3.34 g lead acetate trihydrate were dissolved in 20 mL ethylene glycol monomethyl ether. An appropriate amount of acetic acid was then added into the above solution to adjust the pH, and 0.09 g formamide was added sequentially with constant heating stirring for 30 min. Finally, 1.002 g diacetone and 3.34 g tetrabutyl titanate were added into the mixture solution with water-bath reflux stirring under 80°C for 1 h. The PCT ferroelectric film was deposited by spin coating at 3,000 rpm/s for 30 s and annealed at 500°C for 1 h.

Devices Fabrication

The FTO-coated glass substrates were cleaned by sequential ultrasonic treatment in detergent, acetone, isopropyl alcohol, ethyl alcohol, and deionized water for 30 min, respectively, and dried by a nitrogen stream. The compact TiO_2 ETL was deposited on the FTO substrate by a chemical bath deposition process. The perovskite films were deposited onto PCT and TiO_2-PCT substrates using a method developed in-house. For the surface passivation of PCT film, the [BMIM]BF4-IL dissolved in anhydrous ethanol (3 mg/mL) was spin coated on the PCT layer of the devices. CH_3NH_3I (MAI) at 33.34 mg, 192.5 mg $CH(NH_2)_2I$ (FAI), 77.07 mg $PbBr_2$, 18.2 mg CsI, and 548.6 mg PbI_2 were dissolved in 1 mL dimethylformamide (DMF) and DMSO (4:1, v/v) and then stirred at 60°C for 2 h. Then, spin coating was accomplished under inert atmosphere inside a nitrogen glove box. The procedure was performed by 1,000 rpm for 10 s with the speed of 200 rpm/s, followed by 6,000 rpm at the speed of 2,000 rpm/s for 20 s. At the 5 s before the last spin-coating step, 100 μL chlorobenzene-loaded solution was dropped on the substrate. Then the substrates were put on the top of the hot plate for 60 min at 100°C.

In the fabrication of the hole transport materials (HTM), the 90 mg mL^{-1} Spiro-OMeTAD solution was dissolved in chlorobenzene with dopants of 36 μL 4-*tert*-butylpyridine and 22 μL lithium bis(trifluoromethylsulfonyl) imide of 520 mg mL^{-1} in acetonitrile. The Spiro-OMeTAD solution was spin coated onto the perovskite films at 3,000 rpm for 30 s. Subsequently, ~80 nm Au was evaporated on the top of the cell. For information on the materials used, see the Supplemental Experimental Procedures.

Measurement and Characterization

The J-V curves of the PSCs were tested by the Keithley 2400 source under ambient conditions at room temperature. The illumination intensity was calibrated to 100 mW cm^{-2}. The power output of the AM 1.5G solar simulator was calibrated by a National Renewable Energy Laboratory (NREL) traceable KG5-filtered silicon reference cell. The device area of 0.09 cm^2 was defined by a black metal aperture to avoid light scattering from the metal electrode into the device during the measurement. All of the devices scanned with reverse and forward scan at a scan rate of 0.1 V s^{-1}, the scan step was 0.02 V, and the scan delay time was 50 ms. The incident photon-to-electron conversion efficiency (IPCE) was performed on the QTest Station 2000ADI system (Crowntech). The light source was a 150 W halogen tungsten lamp, and the monochromatic light intensity for the IPCE was calibrated by a reference

silicon photodiode. A TEM image was taken from an FEI Tecnai G^2 F20 microscope. The hysteresis loops and polarization current were investigated on the aixACCT TF Analyzer 2000. Atomic force microscopy (AFM) height images were obtained with a Bruker Multimode 8 in tapping mode. The samples were tested by using a scanning Kelvin probe microscope (SKPM) with a Bruker Metrology Nanoscope VIII AFM in ambient atmosphere. A conductive AFM tip (SCM-PIT/PtIr, Bruker) with a typical spring constant of 2.8 N m^{-1} and a resonance frequency of 75 kHz was used for the measurement. SEM images were obtained by a field emission scanning electron microscope (SU8020) with an accelerating voltage of 5 kV. XRD spectra of samples were collected by a Bruker D8 Advance power diffractometer with a 6.5 kW Cu K_α X-ray radiation (operation at 40 kV and 40 mA). Ultraviolet-visible (UV-vis) spectra were measured using a Shimadzu UV-3600 spectrophotometer. The PCT thin film was prepared on the area of 1 cm^2 FTO glass by spin coating, and the thickness of the PCT film was similar to the PCT ETL of a real device (~300 nm). The conductivity of the samples was measured by using the ST-2258C multifunction digital four-probe tester.

DFT Calculations

Our DFT calculations were performed using the open-source code Quantum ESPRESSO.[43] The exchange correlation interactions are described by PBE for solid (PBEsol) exchange correlation functional.[44] Garrity-Bennett-Rabe-Vanderbilt (GBRV) ultrasoft pseudopotentials (USPPs) were used to treat the electron-ion interactions.[45] A 2a × 2b × 2c supercell of the cubic $FAPbI_3$[46] and a $\sqrt{5}\times\sqrt{5}\times\sqrt{5}$ supercell of $Pb_{0.75}Ca_{0.25}TiO_3$ were used to build the interfacial heterostructures. A vacuum layer of 15 Å was added to avoid the artificial interaction between the neighboring structures. The interfacial heterostructures were optimized with atomic positions being relaxed until the forces on the ions were <0.001 Ry/a.u. Plane-wave cutoffs of 40 and 320 Ry were adopted for expansion of the wave function and density, respectively. A 4 × 4 × 4 Monkhorst-Pack sampling of the Brillouin zone was used to ensure the convergence of the total energy of the heterostructures. All of the atom position and cell parameters were relaxed during the structural relaxation processes.

DATA AND CODE AVAILABILITY

The authors declare that data supporting the findings of this study are available within the article and the Supplemental Information. All other data are available from the Lead Contact upon reasonable request.

SUPPLEMENTAL INFORMATION

Supplemental Information can be found online at https://doi.org/10.1016/j.xcrp.2020.100043.

ACKNOWLEDGMENTS

H.-J.F. was financially supported by the National Natural Science Foundation of China (NSFC) under grants 51972266, 51672214, 11304248, and 11247230; the Natural Science Basic Research Plan in Shaanxi Province of China (program no. 2014JM1014); the Scientific Research Program Funded by Shaanxi Provincial Education Department (program no. 2013JK0624); the Fund Program for the Scientific Activities of Selected Returned Overseas Professionals in Shaanxi Province of China; and the Youth Bai-Ren Project in Shaanxi Province of China. X.C.Z. acknowledges computational support from the University of Nebraska Holland Computing Center.

AUTHOR CONTRIBUTIONS

H.-J.F. conceived the idea and proposed the experimental design. H.-J.F. and C.-X.Q. wrote the manuscript. C-X.Q. performed the device fabrication and data analysis, as well as the preparation of material samples, and characterized their properties. Q.Z. and J.H. carried out all the DFT calculations and analyzed the results. M.-Z.W. and Z.-X.C. conducted the TEM and PFM characterizations of ferroelectric DWs. X.C.Z. modified the language of the article. All of the authors commented on and revised the manuscript.

DECLARATION OF INTERESTS

The authors declare no competing interests.

Received: November 26, 2019
Revised: January 29, 2020
Accepted: February 20, 2020
Published: April 15, 2020

REFERENCES

1. Zheng, Y., Ni, G.X., Toh, C.-T., Tan, C.-Y., Yao, K., and Ozyilmaz, B. (2010). Graphene field-effect transistors with ferroelectric gating. Phys. Rev. Lett. *105*, 166602.

2. Gruverman, A., and Kholkin, A. (2006). Nanoscale Ferroelectrics: Processing, Characterization and Future Trends. Rep. Prog. Phys. *69*, 2443–2474.

3. Evans, J.T., and Womack, R. (1998). An experimental 512-bit nonvolatile memory with ferroelectric storage cell. IEEE J. Solid-State Circuits *23*, 1171–1175.

4. Park, N., Grätzel, M., Miyasaka, T., Zhu, K., and Emery, K. (2016). Towards stable and commercially available perovskite solar cells. Nat. Energy *1*, 16152.

5. Tselev, A., Yu, P., Cao, Y., Dedon, L.R., Martin, L.W., Kalinin, S.V., and Maksymovych, P. (2016). Microwave a.c. conductivity of domain walls in ferroelectric thin films. Nat. Commun. *7*, 11630.

6. Derbenwick, G.F., and Isaacson, A.F. (2001). Ferroelectric memory: on the brink of breaking through. IEEE Circuits and Devices Magazine *17*, 20–30.

7. Salje, E., and Zhang, H. (2009). Domain boundary engineering. Phase Transitions *82*, 452–469.

8. Seidel, J., Martin, L.W., He, Q., Zhan, Q., Chu, Y.-H., Rother, A., Hawkridge, M.E., Maksymovych, P., Yu, P., Gajek, M., et al. (2009). Conduction at domain walls in oxide multiferroics. Nat. Mater. *8*, 229–234.

9. Seidel, J., Fu, D., Yang, S.-Y., Alarcón-Lladó, E., Wu, J., Ramesh, R., III, and Ager, J.W., 3rd (2011). Efficient photovoltaic current generation at ferroelectric domain walls. Phys. Rev. Lett. *107*, 126805.

10. McGilly, L.J., Yudin, P., Feigl, L., Tagantsev, A.K., and Setter, N. (2015). Controlling domain wall motion in ferroelectric thin films. Nat. Nanotechnol. *10*, 145–150.

11. Fäth, M., Freisem, S., Menovsky, A.A., Tomioka, Y., Aarts, J., and Mydosh, J.A. (1999). Spatially Inhomogeneous Metal-Insulator Transition in Doped Manganites. Science *285*, 1540–1542.

12. Seidel, J., Trassin, M., Zhang, Y., Maksymovych, P., Uhlig, T., Milde, P., Köhler, D., Baddorf, A.P., Kalinin, S.V., Eng, L.M., et al. (2014). Electronic properties of isosymmetric phase boundaries in highly strained Ca-Doped $BiFeO_3$. Adv. Mater. *26*, 4376–4380.

13. Crassous, A., Sluka, T., Tagantsev, A.K., and Setter, N. (2015). Polarization charge as a reconfigurable quasi-dopant in ferroelectric thin films. Nat. Nanotechnol. *10*, 614–618.

14. Sluka, T., Tagantsev, A.K., Bednyakov, P., and Setter, N. (2013). Free-electron gas at charged domain walls in insulating $BaTiO_3$. Nat. Commun. *4*, 1808.

15. Schröder, M., Haußmann, A., Thiessen, A., Soergel, E., Woike, T., and Eng, L.M. (2012). Conducting domain walls in lithium niobate single crystals. Adv. Funct. Mater. *22*, 3936–3944.

16. Guyonnet, J., Gaponenko, I., Gariglio, S., and Paruch, P. (2011). Conduction at domain walls in insulating $Pb(Zr_{0.2}Ti_{0.8})O_3$ thin films. Adv. Mater. *23*, 5377–5382.

17. Tian, G., Yang, W., Song, X., Zheng, D., Zhang, L., Chen, C., Li, P., Fan, H., Yao, J., Chen, D., et al. (2019). Manipulation of Conductive Domain Walls in Confined Ferroelectric Nanoislands. Adv. Funct. Mater. *29*, 1807276.

18. Maksymovych, P., Seidel, J., Chu, Y.H., Wu, P., Baddorf, A.P., Chen, L.Q., Kalinin, S.V., and Ramesh, R. (2011). Dynamic conductivity of ferroelectric domain walls in $BiFeO_3$. Nano Lett. *11*, 1906–1912.

19. Ke, W., Fang, G., Liu, Q., Xiong, L., Qin, P., Tao, H., Wang, J., Lei, H., Li, B., Wan, J., et al. (2015). Low-temperature solution-processed tin oxide as an alternative electron transporting layer for efficient perovskite solar cells. J. Am. Chem. Soc. *137*, 6730–6733.

20. Yang, L., Xiong, Y., Guo, W., Zhou, M., Song, K., Xiao, P., and Cao, G. (2018). Manipulation of charge transport in ferroelectric-semiconductor hybrid for photoelectrochemical applications. Nano Energy *44*, 63–72.

21. Wang, M.-Z., Feng, H.-J., Qian, C.-X., He, J., Feng, J.S., Cao, Y.-H., Yang, K., Deng, Z.-Y., Yang, Z., Yao, X., et al. (2019). $PbTiO_3$ as Electron-Selective Layer for High-Efficiency Perovskite Solar Cells: Enhanced Electron Extraction via Tunable Ferroelectric Polarization. Adv. Funct. Mater. *29*, 1806427.

22. Xiao, Z., Meng, W., Wang, J., Mitzi, D.B., and Yan, Y. (2017). Searching for promising new perovskite-based photovoltaic absorbers: the importance of electronic dimensionality. Mater. Horiz. *4*, 206–216.

23. Zhao, Q., Fan, Z.X., Tang, Z.S., Meng, X.J., Song, J.L., Wang, G.S., and Chu, J.H. (2002). Highly (111)-oriented $PbTiO_3$ films prepared by rf planar magnetron sputtering and their optical properties. Surf. Coat. Tech. *160*, 173–176.

24. National Renewable Energy Laboratory (2019). Best Research-Cell Efficiencies. https://www.nrel.gov/pv/assets/images/efficiency-chart.png.

25. Yang, W.S., Noh, J.H., Jeon, N.J., Kim, Y.C., Ryu, S., Seo, J., and Seok, S.I.I. (2015). SOLAR CELLS. High-performance photovoltaic perovskite layers fabricated through intramolecular exchange. Science *348*, 1234–1237.

26. Amat, A., Mosconi, E., Ronca, E., Quarti, C., Umari, P., Nazeeruddin, M.K., Grätzel, M., and De Angelis, F. (2014). Cation-induced band-gap tuning in organohalide perovskites: interplay of spin-orbit coupling and octahedra tilting. Nano Lett. *14*, 3608–3616.

27. Mosconi, E., Ronca, E., and De Angelis, F. (2014). First-Principles Investigation of the TiO_2/Organohalide Perovskites Interface: The Role of Interfacial Chlorine. J. Phys. Chem. Lett. *5*, 2619–2625.

28. Quarti, C., Mosconi, E., Ball, J.M., D'Innocenzo, V., Tao, C., Pathak, S., Snaith, H., Petrozza, A., and De Angelis, F. (2016). Structural and optical properties of methylammonium lead iodide across the tetragonal to cubic phase transition: implications for perovskite solar cells. Energy Environ. Sci. *9*, 155–163.

29. Liu, C., Cai, M., Yang, Y., Arain, Z., Ding, Y., Shi, X., Shi, P., Ma, S., Hayat, T., Alsaedi, A., et al. (2019). A C_{60}/TiOx bilayer for conformal growth of perovskite films for UV stable perovskite solar cells. J. Mater. Chem. A Mater. Energy Sustain. *7*, 11086–11094.

30. Yang, Y., Peng, H., Liu, C., Arain, Z., Ding, Y., Ma, S., Liu, X., Hayat, T., Alsaedi, A., and Dai, S. (2019). Bi-functional additive engineering for high performance perovskite solar cells with reduced trap density. J. Mater. Chem. A Mater. Energy Sustain. *7*, 6450–6458.

31. Liu, X., Ding, X., Ren, Y., Yang, Y., Ding, Y., Liu, X., Alsaedi, A., Hayat, T., Yao, J., and Dai, S. (2018). A star-shaped carbazole-based hole-transporting material with triphenylamine side arms for perovskite solar cells. J. Mater. Chem. C Mater. Opt. Electron. Devices *6*, 12912–12918.

32. Kim, H.S., Mora-Sero, I., Gonzalez-Pedro, V., Fabregat-Santiago, F., Juarez-Perez, E.J., Park, N.G., and Bisquert, J. (2013). Mechanism of carrier accumulation in perovskite thin-absorber solar cells. Nat. Commun. *4*, 2242.

33. Snaith, H.J., Abate, A., Ball, J.M., Eperon, G.E., Leijtens, T., Noel, N.K., Stranks, S.D., Wang, J.T.-W., Wojciechowski, K., and Zhang, W. (2014). Anomalous Hysteresis in Perovskite Solar Cells. J. Phys. Chem. Lett. *5*, 1511–1515.

34. Zhang, C.-C., Wang, Z.-K., Yuan, S., Wang, R., Li, M., Jimoh, M.F., Liao, L.-S., and Yang, Y. (2019). Polarized Ferroelectric Polymers for High-Performance Perovskite Solar Cells. Adv. Mater. *31*, e1902222.

35. Wojciechowski, K., Saliba, M., Leijtens, T., Abate, A., and Snaith, H.J. (2014). Sub-150°C processed meso-superstructured perovskite solar cells with enhanced efficiency. Energy Environ. Sci. *7*, 1142–1147.

36. Sæterli, R., Rørvik, P.M., You, C.C., Holmestad, R., Tybell, T., Grande, T., van Helvoort, A.T.J., and Einarsrud, M.-A. (2010). Polarization control in ferroelectric $PbTiO_3$ nanorods. J. Appl. Physiol. *108*, 124320.

37. Fu, M.S., Ni, L., Liu, X.Q., Chen, X.M., and Zeng, Y.W. (2012). Phase Transition Domains in Ca-based Complex Perovskite Dielectric Ceramics. J. Am. Ceram. Soc. *95*, 2979.

38. Kiguchi, T., Aoyagi, K., Ehara, Y., Funakubo, H., Yamada, T., Usami, N., and Konno, T.J. (2011). Configuration and local elastic interaction of ferroelectric domains and misfit dislocation in $PbTiO_3$/$SrTiO_3$ epitaxial thin films. Sci. Technol. Adv. Mater. *12*, 034413.

39. Feng, H.-J., Deng, W., Yang, K., Huang, J., and Zeng, X.C. (2017). Double Perovskite Cs_2BBiX_6 (B = Ag, Cu; X = Br, Cl)/TiO_2 Heterojunction: An Efficient Pb-Free Perovskite Interface for Charge Extraction. J. Phys. Chem. C *121*, 4471–4480.

40. Chen, B., Yang, M., Zheng, X., Wu, C., Li, W., Yan, Y., Bisquert, J., Garcia-Belmonte, G., Zhu, K., and Priya, S. (2015). Impact of capacitive effect and ion migration on the hysteretic behavior of perovskite solar cells. J. Phys. Chem. Lett. *6*, 4693–4700.

41. van Reenen, S., Kemerink, M., and Snaith, H.J. (2015). Modeling anomalous hysteresis in perovskite solar cells. J. Phys. Chem. Lett. *6*, 3808–3814.

42. Heo, J.H., Song, D.H., Han, H.J., Kim, S.Y., Kim, J.H., Kim, D., Shin, H.W., Ahn, T.K., Wolf, C., Lee, T.W., and Im, S.H. (2015). Planar $CH_3NH_3PbI_3$ Perovskite Solar Cells with Constant 17.2% Average Power Conversion Efficiency Irrespective of the Scan Rate. Adv. Mater. *27*, 3424–3430.

43. Giannozzi, P., Baroni, S., Bonini, N., Calandra, M., Car, R., Cavazzoni, C., Ceresoli, D., Chiarotti, G.L., Cococcioni, M., Dabo, I., et al. (2009). QUANTUM ESPRESSO: a modular and open-source software project for quantum simulations of materials. J. Phys. Condens. Matter *21*, 395502.

44. Perdew, J.P., Burke, K., and Ernzerhof, M. (1996). Generalized Gradient Approximation Made Simple. Phys. Rev. Lett. *77*, 3865–3868.

45. Garrity, K.F., Bennett, J.W., Rabe, K.M., and Vanderbilt, D. (2014). Pseudopotentials for high-through put DFT calculations. Comput. Mater. Sci. *81*, 446–452.

46. Weller, M.T., Weber, O.J., Frost, J.M., and Walsh, A. (2015). Cubic perovskite structure of black formamidinium lead iodide, α-$[HC(NH_2)_2]PbI_3$ at 298 K. J. Phys. Chem. Lett. *6*, 3209–3212.

Cell Reports Physical Science, Volume *1*

Supplemental Information

Domain Wall Conduction in Calcium-Modified Lead Titanate for Polarization Tunable Photovoltaic Devices

Chong-Xin Qian, Hong-Jian Feng, Qiang Zhang, Jiawei He, Zi-Xuan Chen, Ming-Zi Wang, and Xiao Cheng Zeng

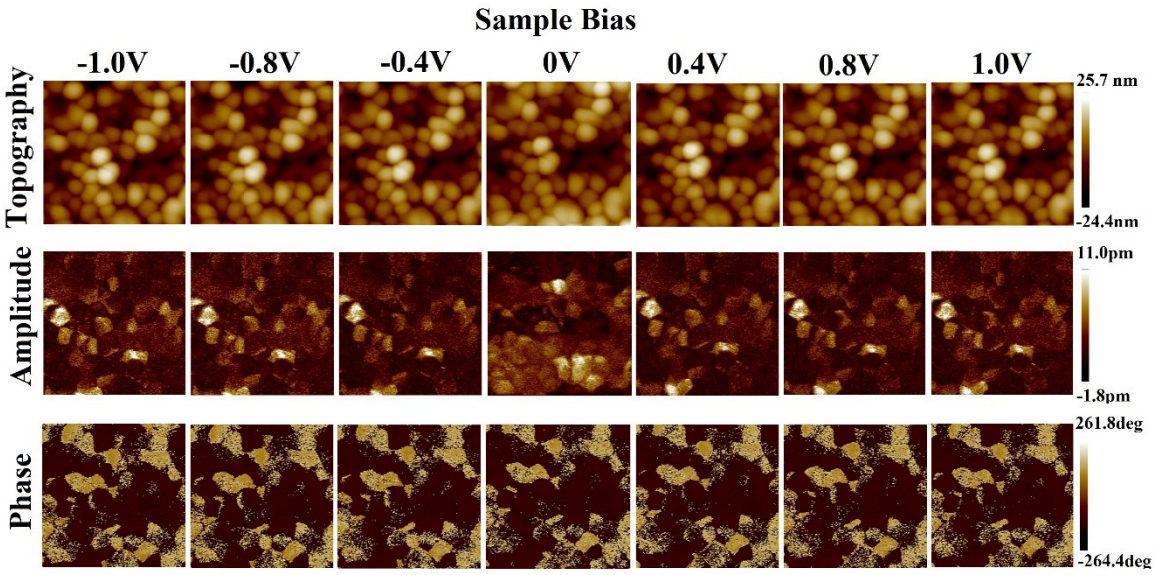

Figure S1. The PCT film surface topography, amplitude and the phase images under the bias voltage arrange from 0 to ± 1V, respectively.

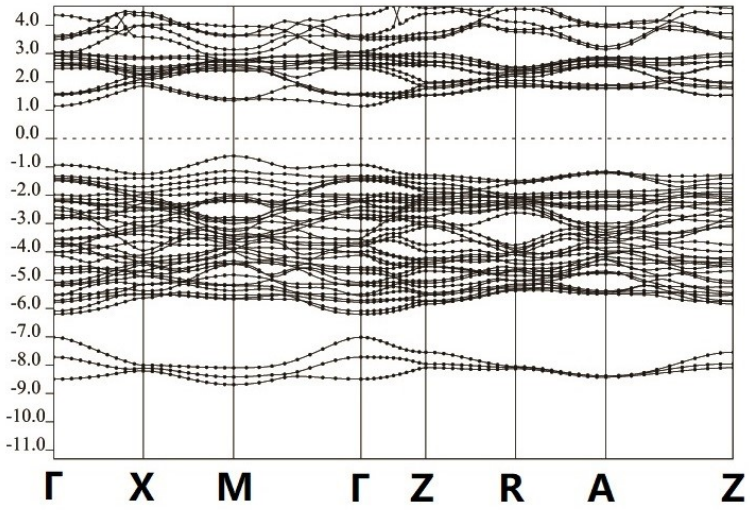

Figure S2. Computed electronic band structure calculated by PBE/GGA.

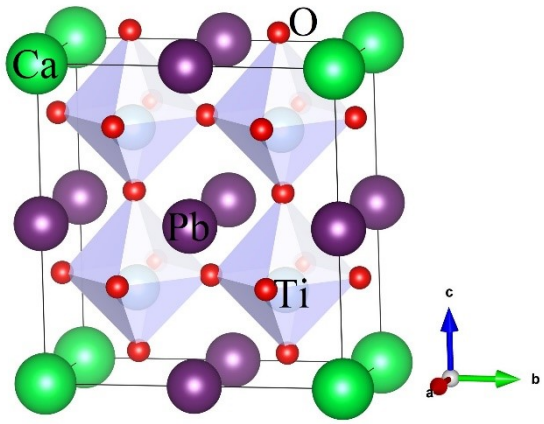

Figure S3. The $Pb_{0.8}Ca_{0.2}TiO_3$ cell structure.

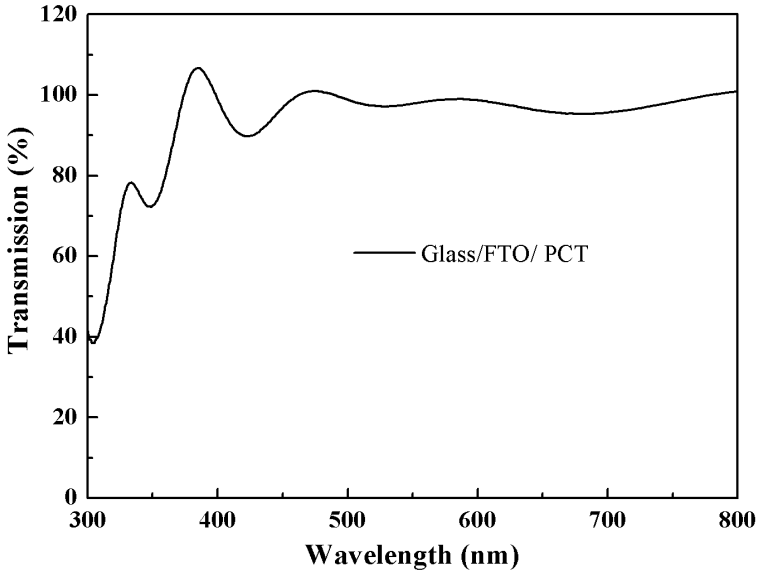

Figure S4. Optical transmission spectra of PCT film.

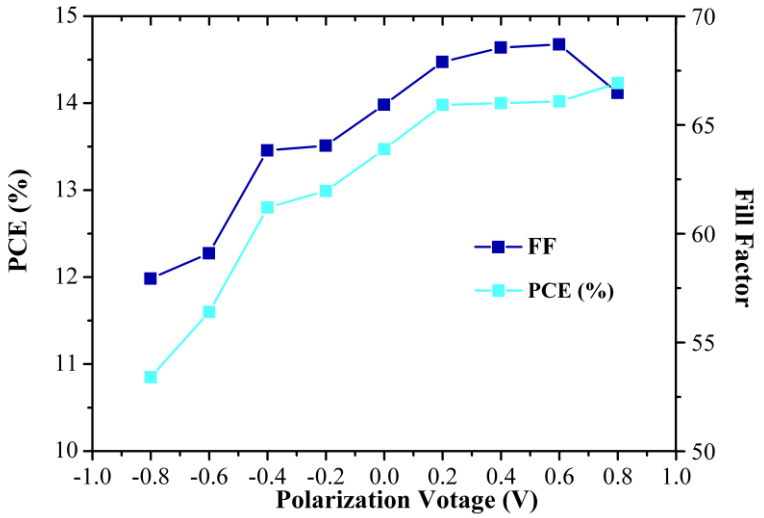

Figure S5. The PCE and the Fill Factors measured after poling with different polarization bias.

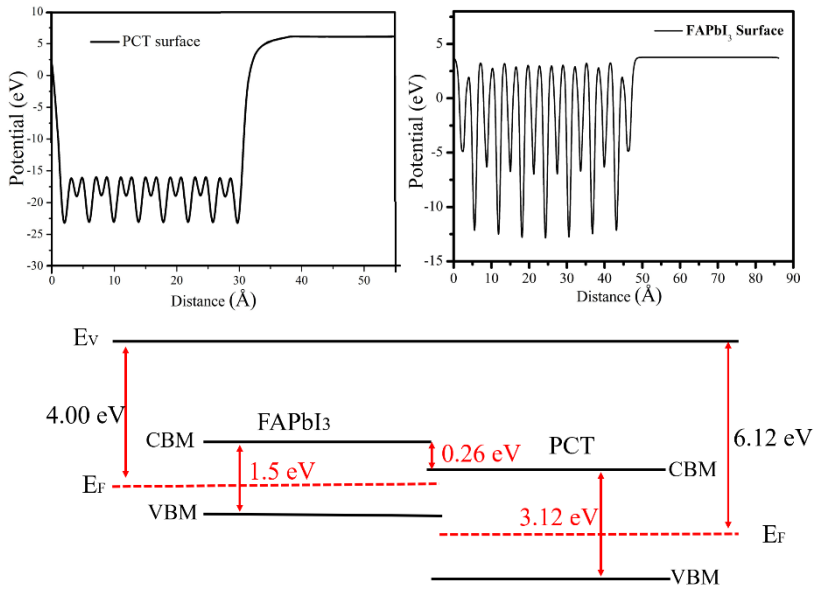

Figure S6. Conduction band offset schematic of $FAPbI_3$/PCT heterostructure based on work functions computed based on HSE06 functional with respect to the vacuum level.

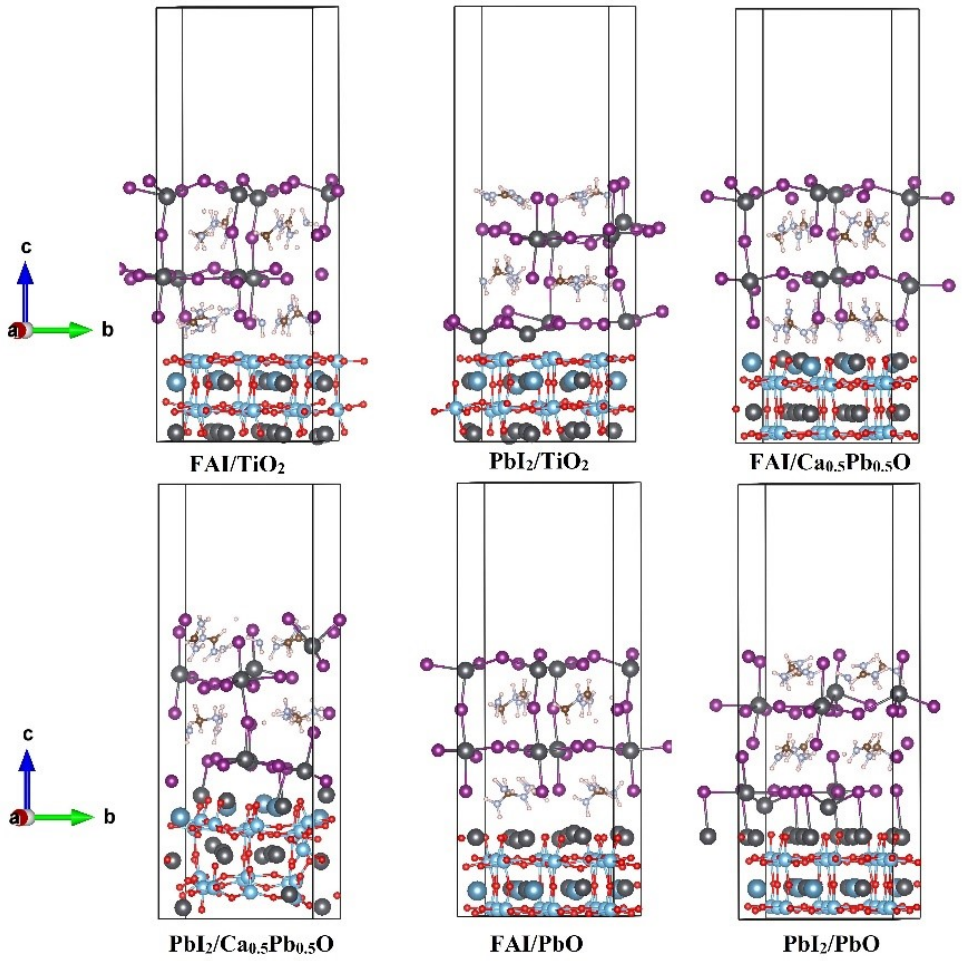

Figure S7. Six different relaxed interfaces for PCT/perovskite heterojunction.

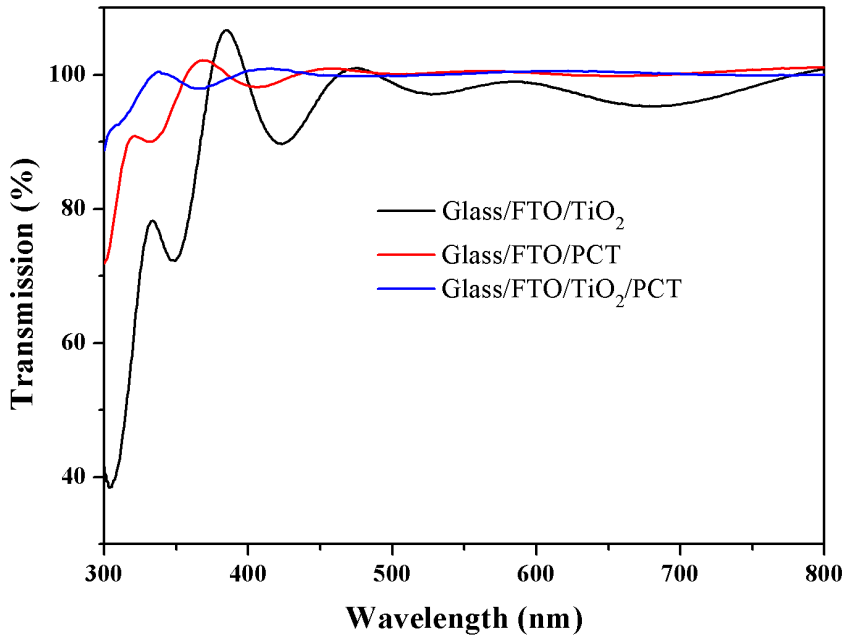

Figure S8. Measured transmission of different ETLs deposited on Glass/FTO substrate.

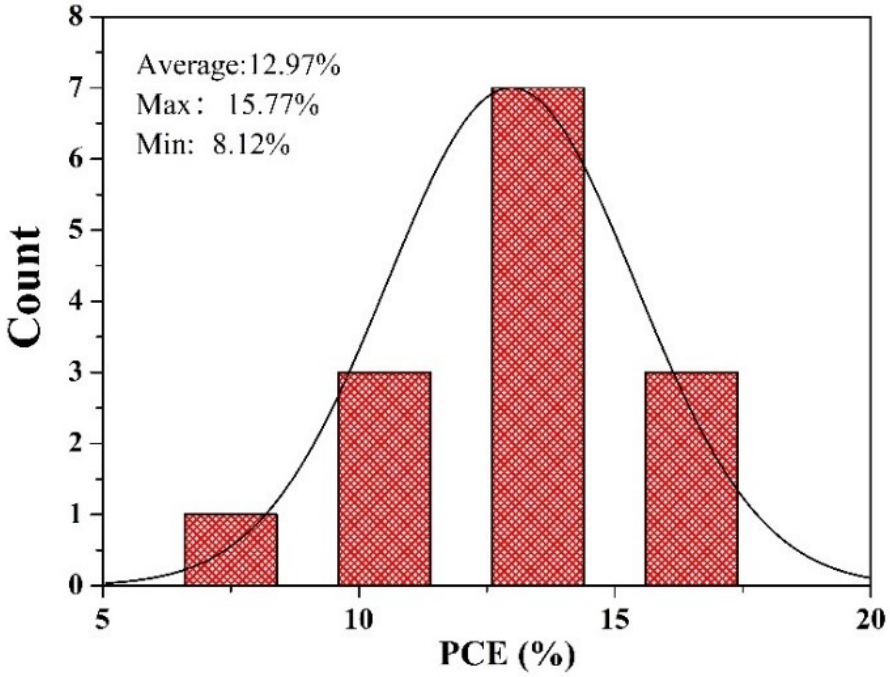

Figure S9. The histogram of the PCE of the passivated PCT-based devices.

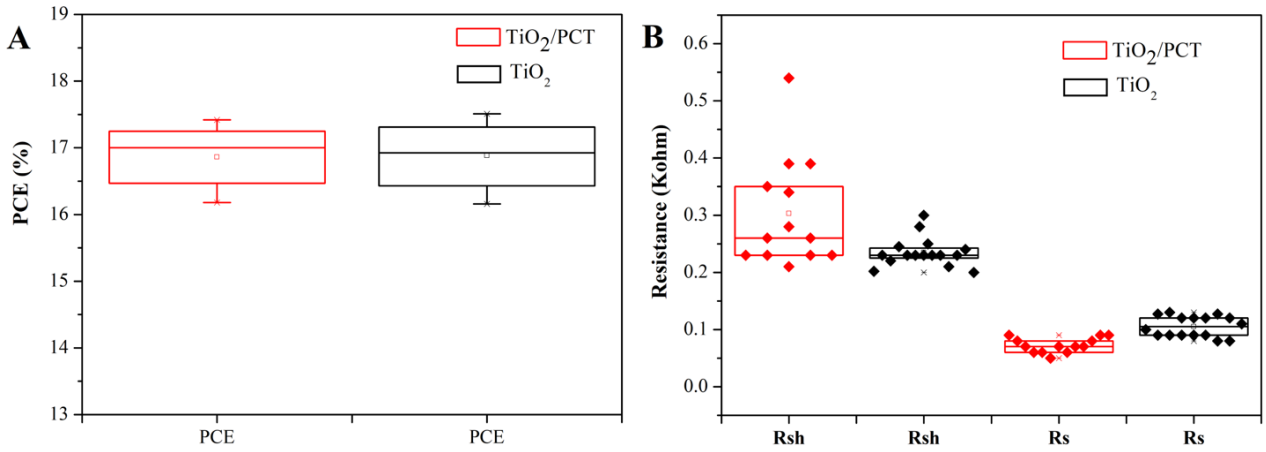

Figure S10. Statistics of the device performance PCE (A) and (B) the series resistance (R_s) and shunt resistance (R_{sh}) of PSCs with TiO_2 and TiO_2/PCT as ETLs, respectively. The median and mean are represented by the line dividing the boxes and the open square symbols, respectively. The cross symbols represent the maximum and minimum values.

Table S1. Upon the different poling bias, the parameters measured from reverse direction of PCT based device.

Poling bias	V_{oc}(V)	J_{sc}(mA/cm^2)	FF(%)	PCE(%)
Poling +0.8V	1.08	23.16	63.91	15.98
Poling +0.6V	0.98	21.80	66.48	14.08
Poling +0.4V	1.04	19.59	66.42	13.53
Poling +0.2V	0.98	20.85	65.93	13.47
No Poling	0.98	20.70	64.05	12.99
Poling -0.2V	0.98	20.56	63.83	12.85
Poling -0.4V	0.96	20.45	59.11	11.60
Poling -0.6V	0.94	19.92	57.94	10.85
Poling -0.8V	0.96	17.01	51.61	8.43

Table S2. The key parameters of different ETL devices.

ETL		V_{oc}(V)	J_{sc} (mA/cm^2)	FF (%)	PCE (%)
TiO_2	Reverse	1.1	20.74	76.74	17.51
	Forward	1.04	20.78	69.96	15.12
PCT	Reverse	1.08	23.16	63.91	15.99
	Forward	0.98	23.05	66.39	14.99
TiO_2/ PCT	Reverse	1.05	23.11	75.29	18.28
	Forward	1.04	22.81	68.73	16.34

Supplemental Experimental Procedures

Materials

Lead acetate trihydrate, calcium acetate, tetrabutyl titanate, ethylene glycol monomethyl ether, diacetone, formamide, acetic acid and titanium tetrachloride were purchased from Sinopharm Chemical Reagent Co. Ltd. MAI (99.99%), FAI (99.99%), PbI_2 (99.9985%), 2,2,7,7-Tetrakis (N,N-di-p-methoxyphenylamine)-9,9-spirobif-luorene (Spiro-OMeTAD), Lithium bis (trifluoro-methanesulfonyl) imideanhydrous (Li-TFSI) and 4-tertbuthylpyridine (tBP) were purchased from Xi'an Poled Electronic Technology Co. Ltd. CsI, $PbBr_2$, acetonitrile and chlorobenzene were purchased from Aladdin. All precursor materials and solvents were used as received without further purification.

The charge displacement curve between the lowest triplet states and the ground states

The charge displacement curve (CDC)

The plane-averaged charge difference Δq can be defined by

$$\Delta q = \int_{-\infty}^{+\infty} \int_{-\infty}^{+\infty} (\rho_{FA/BTO} - \rho_{FA} - \rho_{BTO}) dxdy \qquad (1)$$

Where $\rho_{FA/BTO}$, ρ_{FA} and ρ_{BTO} are charge density of $FAPbI_3$/BTO heterostructure, $FAPbI_3$ slab and BTO slab, respectively. The CDC curve can be calculated by integrating Δq along z axis

$$\Delta Q = \int_{-\infty}^{z} \Delta q dz \qquad (2)$$

The CDC curve between the lowest triplet states and the ground states.

The CDC curve ΔQ between the lowest triplet states and the ground states can be calculated by

$$\Delta Q = \int_{-\infty}^{\infty} dx \int_{-\infty}^{\infty} dy \int_{-\infty}^{z} (\rho_L - \rho_G) dz \qquad (3)$$

Where ρ_L and ρ_G denote the electron density of lowest triplet states and ground states in the real space, respectively.